Petroleum Science 22 (2025) 1876–1888

Contents lists available at ScienceDirect

Petroleum Science

journal homepage: www.keaipublishing.com/en/journals/petroleum-science

Original Paper

DLVO-based estimates of critical water saturation of shale: A case study of the lower Silurian Longmaxi shale in Sichuan Basin

Cheng-Xiang Wan [a, b, c, *], Xu-Sheng Guo [a, b, c], Bao-Jian Shen [a, b, c], Yan Song [d], Peng-Wei Wang [a, b, c], Ru-Yue Wang [a, b, c]

[a] State Key Laboratory of Shale Oil and Gas Enrichment Mechanisms and Efficient Development, Beijing, 102206, China
[b] Sinopec Key Laboratory of Shale Oil/Gas Exploration & Production Technology, Beijing, 102206, China
[c] Sinopec Petroleum Exploration and Production Research Institute, Beijing, 102206, China
[d] Unconventional National Gas Institute, China University of Petroleum (Beijing), Beijing, 102249, China

ARTICLE INFO

Article history:
Received 13 July 2024
Received in revised form
10 September 2024
Accepted 3 March 2025
Available online 6 March 2025

Edited by Jie Hao and Meng-Jiao Zhou

Keywords:
Water film
Pore structure
Critical water saturation
Shale gas
Longmaxi shale

ABSTRACT

Shale gas is an important unconventional resource, and shale reservoirs typically contain both water and gas fluids. Water can occupy the shale gas storage space, reduce the flow capacity of shale gas, and even completely seal off the shale gas. When the shale develops an effective sealing capacity, the water saturation of the shale reaches a threshold value which can be measured using physical simulation experiments. However, limited research has been conducted on the quantitative calculation of critical water saturation. In order to obtain the critical water saturation of shale, this paper proposes a theoretical calculation method to estimate the critical water saturation of shale based on DLVO (Derjaguin-Landau-Verwey-Overbeek) theory. Two shale samples from the Longmaxi Formation in the Sichuan Basin with different total organic carbon (TOC) were selected for gas adsorption experiments to characterize the pore structure of the organic matter and inorganic matter of the shale. Based on the established theoretical and geological models, the critical water film thickness and critical water saturation of pores with different pore sizes were calculated. Taking the boundary conditions into account, the critical water saturation of the two shale samples was ultimately determined. The results showed that inorganic pores occupied 81.0% of the pores of the shale with a TOC of 0.89%, and their dominant pore sizes were dominated by mesopores around 40 nm; inorganic pores occupied 48.7% of the pores of the shale with a TOC of 4.27%, and their dominant pore sizes were dominated by micropores and mesopores around 0–20 nm and 40 nm. As the pore size increased, the corresponding critical water film thickness also increased, and the critical water saturation was normally distributed in the pore size range centered at about 10 nm. The distribution of critical water saturation in inorganic pores with different pore sizes was in the range of about 63%–76%, and the critical water saturation of shale with a TOC of 0.89% and shale with a TOC of 4.27% were calculated to be 41.7% and 32.7%, respectively. The method proposed in this study accurately calculates the critical water saturation of shale and effectively distinguishes the differences critical water saturation between shales with different TOC. Further, shale gas reservoirs can be finely characterized by comparing with the original water saturation of shale layers. This study is of great scientific significance to shale gas exploration and development, and even to the field of CO_2 geological storage.

1. Introduction

Shale formation is a very important source of energy, not only because it is a hydrocarbon source rock, but also it can be used as a reservoir for hydrocarbons (Cai et al., 2023; Hu et al., 2024; Liu et al., 2023). In the context of CCUS, the global energy consumption structure shows a trend of high carbon energy to low carbon energy and clean energy. And shale gas, as a clean energy source, has gradually increased its share in the energy consumption structure (Xue et al., 2023). The Longmaxi shale is an important shale gas reservoir and is considered to have no water content or ultra-low water saturation characteristics, resulting in little attention paid to its water saturation. However, the saturation evaluation

* Corresponding author.
E-mail address: 18811155022@163.com (C.-X. Wan).

https://doi.org/10.1016/j.petsci.2025.03.003

for fine-grained sediments has always been a focus and difficulty of research, which is of great significance for shale physical property evaluation and shale gas exploration and development (Wang et al., 2021; Zhu et al., 2022, 2023). Due to the presence of water, the storage and seepage behavior of methane gas in shale is significantly affected (Guo et al., 2023, 2024). Previous studies have shown that the methane adsorption capacity of shale under water-bearing conditions will decrease by 40%–90% (Ross and Bustin, 2009; Gasparik et al., 2014; Li et al., 2016a), and the permeability will decrease by 10%–90%, compared with water-free conditions (Li et al., 2015; Tan et al., 2021). When the water saturation is higher than a certain value, which generally called the critical water saturation, the gas flow ability will be completely restricted. This phenomenon has been confirmed in many gas-water two-phase seepage experiments. Zhang's study pointed out that there exists a critical water saturation in shale, and when the shale water saturation reaches the critical value, the largest connecting pore throats in the shale pore network are blocked by water, and the breakthrough pressure of shale will be steeply increased, thus the gas will be effective sealed by the shale (Fig. 1) (Zhang and Yu, 2016, 2019). However, the critical water saturation of shale obtained through physical simulation experiments has significant uncertainty and requires a significant amount of time, samples, and experimental funding, and few studies have been reported on the quantitative calculation of the critical water saturation of shale.

There are many methods, such as centrifugal-NMR (Nuclear magnetic resonance) experiment, MDS (Molecular dynamics simulation) and DLVO method, to study the micro-distribution characteristics of water in shale gas pores. The centrifugal-NMR can be used to distinguish the adsorbed water and bound water content in shale, but it is not applicable to the concept of critical water saturation in this study (Li et al., 2019, 2023, 2024; Jiao et al., 2025). MDS can effectively study fluid behavior in nanopores and has good visualization effects, but it can usually only be calculated in very small pore sizes (usually only a few nanometers), and the establishment of molecular models involves subjectivity (Yu et al., 2019, 2021; Xu et al., 2020). The water film theory is an effective method to study the distribution behavior and characteristics of water at the nanoscale. The famous DLVO theory was proposed by Derjaguin and Landau (1941), and Verwey and Overbeek (1948). There is an interaction force between a thin film of water on the surface and the solid surface, called the disjoining pressure $\Pi(h)$. Disjoining pressure is a major factor in determining the thickness and stability of a thin water film and usually consists of three components: intermolecular forces, electrostatic forces, and structural forces (Derjaguin et al., 1987). Combining the disjoining pressure and Kelvin thermodynamic equations, the relationship between humidity and water film thickness can be established when water undergoes capillary condensation in pores of different pore sizes, thus the relationship between the water film thickness and the water saturation of shale can be further established (Nikolai et al., 2000; Li et al., 2017). The residual water film thickness of different pore size pores after being displaced by gas can be well described by the capillary force equation and disjoining pressure equation, so as to understand the distribution characteristics of adsorbed water film in shale. In addition, the water film theory has also been applied to the study of CO_2 gas sequestration. Tokunaga (2012) predicted that the water film thickness of adsorbed water in CO_2 gas reservoirs is usually less than 10 nm, and Zhao (2021) computed the water film thicknesses in pores of different sizes, which revealed that the CO_2 transport behavior under geologic reservoir conditions has a water film thickness dependence and provide useful information for reservoir and cap layer optimization and evaluation of CO_2 storage effectiveness.

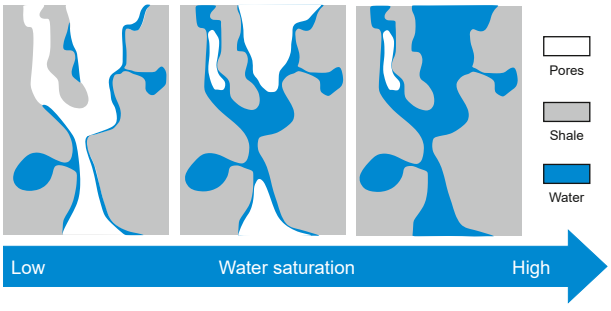

Fig. 1. Schematic diagram of water filling process in rock pores (Modified from Zhang et al. (2019))

It is well known that shale is an organic-inorganic complex that is extremely inhomogeneous (Curtis et al., 2011). The distribution of water in shale is particularly complex, influenced by the wettability of different components. In general, the distribution of water in shale is mainly influenced by inorganic minerals, especially clay minerals. Clay minerals are usually negatively charged to varying degrees, and the interaction between water molecules with polarity and clay minerals is much stronger than that between water molecules and organic matter due to hydrogen bonding and electrostatic forces (Li et al., 2016b; Yang et al., 2020). On the contrary, high-maturity organic matter of Longmaxi shale is hydrophobic. The ability of organic matter to adsorb water usually depends on the presence of hydrophilic functional groups. The density of functional groups on the surface of organic matter decreases significantly with increasing thermal maturity. The oxygen-containing functional groups of organic matter in high-maturity shales are almost completely detached, and the organic matter surface lacks active adsorption sites and may be covered by hydrophobic asphalt; therefore, it is generally believed that it is difficult for water to enter the organic pore space of these high-maturity shales (Hu et al., 2014, 2015; Cheng et al., 2022). Although more and more studies suggest that a certain amount of water may still be present in the organic pores of high-maturity shales (Clarkson and Bustin, 2000; Charrière and Behra, 2010; Gu et al., 2016; Cheng et al., 2018; Zou et al., 2020; Xing et al., 2024), since the formation of organic matter pores accompanied by hydrocarbon production and expulsion carries water out of the organic pores, the trace amount of water inside the organic matter may not be able to stay in real situations (Cheng et al., 2019; Wang et al., 2022; Gao et al., 2022; Wu et al., 2023).

2. Theory

2.1. DLVO theory

2.1.1. Intermolecular force

The intermolecular force mainly includes orientation, induced and dispersion forces, which can be manifested as either gravitational or repulsive forces, and their direction is related to the polarity of the solid-liquid molecules. The formula for calculating the van der Waals force between different geometrical models is different, and the formula for the van der Waals force between two parallel interfaces is given by Eq. (1) (Gregory, 1975):

$$\Pi_{\mathrm{m}}(h) = -\frac{A_{\mathrm{gws}}\left(15.96\frac{h}{l}+2\right)}{12\pi h^3\left(1+5.32\frac{h}{l}\right)^2} \tag{1}$$

where $\Pi_{\mathrm{m}}(h)$ is the van der Waals force, MPa; A_{gws} is the Hamaker constant for gas-liquid-solid three-phase interaction, J; h is the

water film thickness, nm; l is the wavelength of molecular force, nm.

The Hamaker constant is important for the calculation of intermolecular forces, which represent the interaction energy between multiphase substances. The Hamaker constant can be calculated by simplifying Eq. (2) (Hough and White, 1980; Prieve and Russel, 1988).

$$A_{132} \approx \left(\sqrt{A_{11}} - \sqrt{A_{33}}\right)\left(\sqrt{A_{22}} - \sqrt{A_{33}}\right) \tag{2}$$

where A_{132} is the Hamaker constant for the interaction of three different media systems, which is A_{gws} in this paper, J; A_{11} is the Hamaker constant for gas/gas in vacuum, J; A_{33} is the Hamaker constant for water/water in vacuum, J; A_{22} is the Hamaker constant for solid/solid in vacuum, J. The object of this paper is Longmaxi shale, so the three-phase system is methane-water-shale (quartz or clay minerals).

In addition, the Hamaker constant consists of both zero and high frequency components (Eq. (3)). The magnitude of the Hamaker constant depends mainly on the static dielectric constant and refractive index of the substance.

$$A_{131} = A_{\nu=0} + A_{\nu>0} = \frac{3}{4}kT\left(\frac{\varepsilon_1 - \varepsilon_3}{\varepsilon_1 + \varepsilon_3}\right)^2 + \frac{3h\nu_e}{16\sqrt{2}}\frac{\left(n_1^2 - n_3^2\right)^2}{\left(n_1^2 + n_3^2\right)^{3/2}} \tag{3}$$

where Hamaker constant A_{131}: the same substance 1 mediates the interaction of substance 3 (substance 3 mediates between two substances l), J; $A_{\nu=0}$: zero-frequency Hamaker constant, J; $A_{\nu>0}$: high-frequency Hamaker constant, J; ε: static dielectric constant, F/m; h: Planck's constant, taken as 6.63×10^{-34} J·s; n: refractive index.

Under room temperature conditions (T = 298.15 K and P = 0.1 MPa), $A_{gg} \approx 0$ J, $A_{ww} \approx 3.67 \times 10^{-20}$ J and $A_{ss} \approx 2.0 \times 10^{-19}$ J can be calculated by Eq. (3). Further, according to Eq. (2), the value of A_{gws} is approximately -4.9×10^{-20} J.

2.1.2. Electrostatic force

Electrostatic force is a long-range force. The limiting distance of the range of electrostatic force is the Debye length, and electrostatic force is generated by the interaction between charged surfaces, which is closely related to the structure of the double electric layer at the interface of the medium (Israelachvili, 2011). The electrostatic force formed by the interaction of two planes with a low constant potential in a 1:1 electrolyte solution is given by Eq. (4) (Hua et al., 2015; Gregory, 1975; Zeng et al., 2020):

$$\Pi_e(h) = \frac{2\varepsilon_0\varepsilon\kappa^2\left[\left(e^{+\kappa h} + e^{-\kappa h}\right)\psi_1\psi_2 - \left(\psi_1^2 + \psi_2^2\right)\right]}{\left(e^{+\kappa h} - e^{-\kappa h}\right)^2} \tag{4}$$

where $\Pi_e(h)$ is the electrostatic force, $N \cdot m^{-2}$; h is the thickness of the water film, m; ε_0 is vacuum/absolute dielectric constant, taken as 8.85×10^{-12} F/m; ε: dielectric constant of water, F/m; ψ: surface potential, V; κ^{-1}: Debye length, m; e: electron charge, taken as 1.602×10^{-19} C.

The Debye length is given as:

$$\kappa^{-1} = \left(z^2\varepsilon_0\varepsilon k_B T \Big/ 2\rho_\infty e^2\right)^{1/2} \tag{5}$$

where κ^{-1} is the Debye length, nm; z is the solution ion valence state; k_B is Boltzmann's constant, taken as 1.381×10^{-23}; ρ_∞ is the cation concentration per unit volume of solution, number/m^3.

The key parameters in the electrostatic force formula are the Debye length and surface potential. The calculation of the Debye length needs to know the cation concentration in the aqueous solution, and the main type of Longmaxi shale formation water is NaCl type, so monovalent cations dominate in the shale formation water. By converting the mineralization of formation water from PY1 and PY3 wells with good preservation conditions, the cation concentration obtained was between 0.4 and 0.8 (Zhang et al., 2021). In this paper, the cation concentration of aqueous solution was taken as 0.5 M, so the length of Debye at room temperature in this system was 0.43 nm. The surface potential of inorganic minerals is only slightly higher than ±35 mV in high concentration NaCl solutions (10^{-3}–10^{-2} M) (Hunter and Wright, 1971; Hunter, 1981), and the surface potential typically reaches its minimum value when the ion concentration exceeds 0.3 M (Vinogradov and Jackson, 2015). Referring to the studies of Rodríguez and Araujo (2006) and Vinogradov and Jackson (2015) on the surface potential of inorganic minerals in different electrolyte solutions, in this paper the solid-liquid surface potential is taken to be −10 mV. The same law exists for the potential at the gas-liquid interface, so the gas-liquid surface potential is taken to be −20 mV according to the results of the study of the surface potential of NaCl solution by Li (1991).

2.1.3. Structural force

Structural force is a short-range force that can be either repulsive or gravitational, depending on the wettability of the solid surface. It mainly acts on the thickness of a few molecular layers closest to the solid surface. This force is usually thought to be related to hydrogen bonding in water molecules. In this study, the interaction of the charges on the surface of polar minerals (e.g., clay minerals) on the shale surface with the hydrogen bonding of the water molecules results in the directional arrangement of the water molecules close to the shale surface to form a layer of strongly bound water molecules, which in turn has some effect on the thickness of the water film. The structural forces can be calculated by the semi-empirical Eq. (6) (Churaev, 1995):

$$\Pi_s(h) = Ke^{-\frac{h}{\lambda}} \tag{6}$$

where $\Pi_s(h)$ is the structural force, MPa; K is the solid surface correlation coefficient, taking the value related to the wetting angle, dyn/cm^2, when the wetting angle is less than 20°, $K > 0$, when the wetting angle is 20°–40°, $K \approx 0$, when the wetting angle is more than 40°, $K < 0$; λ is the characteristic length of the water molecule, 1–2 nm. Referring to the study of Li et al. (2017) on the structural force of the water film in the Longmaxi shale, the solid surface correlation coefficient is taken as 1.5×10^7 Pa, and the water molecule characteristic length is taken as 1 nm. The relevant parameters and values are listed in Table 1.

2.2. Theoretical calculation models

2.2.1. Flat surface

The simplest water film model is a thin water film on a flat surface (Fig. 2(a)), and the interaction force between the thickness of the thin water film and the solid surface can be quantified calculated by the disjoining pressure $\Pi(h)$. In general, the effective disjoining pressure on a flat surface is the combined force of three forces (Derjaguin et al., 1987), given by Eq. (7):

$$\Pi_{flat}(h) = \Pi_m(h) + \Pi_e(h) + \Pi_s(h) \tag{7}$$

where $\Pi_{flat}(h)$ is the disjoining pressure of water film on flat surface, MPa.

Table 1
Relevant parameters of disjoining pressure and simulation process.

Parameter	Symbol	Unit	Value
Temperature	T	K	298.15
Pressure	P	MPa	0.101
Wavelength of molecular force	l	nm	100
Static dielectric constant of gas	ε_g	F/m	1.00083
Refractive index of gas	n_g	Dimensionless	1.00041
Static dielectric constant of liquid	ε_l	F/m	82.1117
Refractive index of liquid	n_l	Dimensionless	1.33776
Planck's constant	h	J·s	6.63×10^{-34}
Electronic absorption frequency	ν_e	s^{-1}	3×10^{15}
Hamaker constant for gas/gas in vacuum	A_{gg}	J	0
Hamaker constant for water/water in vacuum	A_{ll}	J	3.67×10^{-20}
Hamaker constant for solid/solid in vacuum	A_{ss}	J	2.0×10^{-19}
Hamaker constant for the interaction of methane-water-shale system	A_{gws}	J	-4.9×10^{-20}
Vacuum/absolute dielectric constant	ε_0	F/m	8.85×10^{-12}
Debye length	κ^{-1}	nm	0.43
Electron charge	e	C	1.602×10^{-19}
Solution ion valence state	z	Dimensionless	1
Boltzmann's constant	k_B	Dimensionless	1.381×10^{-23}
Cation concentration per unit volume of solution	ρ_∞	number/m^3	3.011×10^{26}
Surface potential of solid-liquid	ψ_1	mV	−10
Surface potential of gas-liquid	ψ_2	mV	−20
Solid surface correlation coefficient	K	Pa	1.5×10^7
Characteristic length of the water molecule	λ	nm	1
Gas-water surface tension	σ	N/m	0.073
Contact angle	θ	°	0

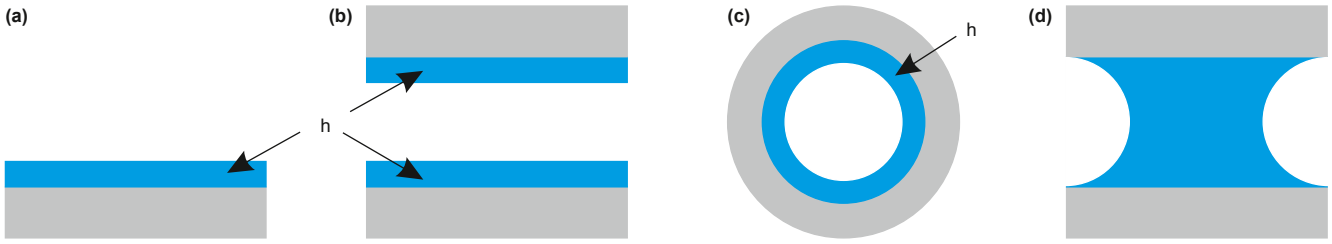

Fig. 2. Schematic diagram of water film in different models and capillary water in slit pore.

2.2.2. Capillary pores

Fig. 2(c) characterizes the distribution of the water film inside a capillary pore, where h is the water film thickness and r is the capillary radius. Unlike the water film on a flat surface (Fig. 2(a)), the water film inside a capillary pore exhibits a curved liquid surface. Therefore, the water film is subject to an additional capillary force P_c in addition to the disjoining pressure. It should be noted that the additional capillary force is the capillary force formed by the curved liquid surface, not the capillary force formed by the column surface. Also, the disjoining pressure becomes $r/(r-h)\Pi(h)$ instead of $\Pi(h)$ (Davide and Victor, 2012).

Therefore, the effective disjoining pressure within the circular tube hole model can be calculated by Eq. (8):

$$\Pi_{\text{tube}}(h) = \frac{r}{r-h}\Pi_{\text{flat}}(h) + P_c = \frac{r}{r-h}\Pi_{\text{flat}}(h) + \frac{\sigma\cos\theta}{r-h} \tag{8}$$

where $\Pi_{\text{tube}}(h)$ is the disjoining pressure of water film inside the capillary pore, MPa; σ is the gas-water surface tension, mN/m; θ is the contact angle, degree.

2.2.3. Slit pores

Fig. 2(b) characterizes the distribution of the water film in a slit pore, where h is the water film thickness and H is the width of the slit pores. The disjoining pressure on the water film adsorbed on slit pores is more complex. The analysis of the disjoining pressure on the water film shows that in addition to the interaction force between the water film and the wall on the same side, there is also the interaction force between the water film and the wall on the other side and the water film on the other side (Tuller et al., 1999; Li et al., 2016b). Therefore, the calculation formula for the disjoining pressure applied to the water film in slit pores is as follows:

$$\Pi_{\text{slit}}(h) = \Pi_1(h) + \Pi_2(h) + \Pi_3(h) \tag{9}$$

$$\Pi_1(h) = \Pi_m(A_{gws}, h) + \Pi_e(h) + \Pi_s(h) \tag{10}$$

$$\Pi_2(h) = \Pi_m(A_{gws}, H-h) \tag{11}$$

$$\Pi_3(h) = -\Pi_m(A_{wgw}, H-2h) \tag{12}$$

where $\Pi_1(h)$ is the interaction force between water film and the wall on the same side, MPa; $\Pi_2(h)$ is the interaction force between the water film and the wall on the opposite side, MPa; $\Pi_3(h)$ is the interaction force between the water film and the opposite side water film, MPa. The intermolecular forces of $\Pi_1(h)$ and $\Pi_2(h)$ are all the disjoining pressure between the wall and the water film, which is manifested as gas-liquid-solid three-phase action and the Hamaker constant is A_{gws}. The intermolecular force of $\Pi_3(h)$ is the interaction force between the two water films, which is a liquid-gas-liquid interaction with the Hamaker constant of A_{wgw}.

2.3. Stability of water film

As the thickness of the water film in the pore space increases, the distance between the water films will become smaller and smaller, and the forces between the water films will become larger and larger. When the interaction forces within the system cannot maintain the structure of the water film, the water film suddenly loses its stability and capillary condensation occurs immediately (Derjaguin and Churaev, 1992; Tuller et al., 1999; Zhang et al., 2017a) (Fig. 2(d)). When water film undergoes capillary condensation to form capillary water, the derivative of disjoining pressure on water film thickness is zero (Iwamatsu and Horii, 1996; Churaev et al., 2000; Bucior, 2004; Yu et al., 2019). It corresponds to the inflection point of the correlation curve between disjoining pressure and water film thickness:

$$\frac{\partial \Pi(h)}{\partial h} = 0 \tag{13}$$

Therefore, the thickness of the water film when capillary condensation occurs is the critical water film thickness, and the corresponding water saturation is the critical water saturation.

3. Material and method

3.1. Sample information

The two sets of samples in this paper are selected from fresh cores of typical shale gas wells of the Silurian Longmaxi shale Formation in southern Sichuan. They are respectively selected from the upper and lower shale layers of the Longmaxi Formation gas bearing shale. TOC is one of the most important geological parameters of shale. TOC data were obtained by the standard of GB/T 19145-2003. 1 g of 200 mesh powder samples were prepared for acid treatment by hydrochloric acid at 80 °C for 2 h. After the carbonate minerals and HCl were almost completely reacted, the samples were placed in a dry pan, the residual HCl was washed away with distilled water, and the samples were put in a thermostat at 80 °C for 24 h. Finally, the TOC were tested in a LECO CS-200 carbon and sulfur analyzer. XRD testing is also essential for shale. The fragments of N1 and N2 samples were manually ground to 200 mesh and coated on a glass slide for XRD analysis. Then, based on TOC and XRD data, the lithofacies types of shale can be identified. The basic information of the samples is shown in Table 2.

3.2. FE-SEM

FE-SEM is used to visualize the pore morphology characteristics in the shale, so as to establish a more accurate pore geological model of the shale. The observation of pores and microstructure of N1 and N2 samples is carried out through FE-SEM. Shale samples of approximately 1 cubic centimeter need to be prepared in advance. After polishing and Au powder covering treatment, the surface of shale can be observed under scanning electron microscopy. Finally, the pore structure of shale can be qualitatively or quantitatively characterized through high-resolution scanning electron microscopy photos.

Table 2
Basic information of shale samples.

Sample number	TOC, %	Clay, %	Silicious, %	Carbonate, %	Lithofacies
N1	0.89	54	46	0	Clay shale
N2	4.27	19	67	14	Siliceous shale

3.3. Preparation of kerogen

Shale is an organic-inorganic complex, and the distribution characteristics of water in organic and inorganic pores differ significantly. In order to calculate the critical water saturation of shale more accurately, it is necessary to distinguish the organic and inorganic components in shale. The organic components in shale can be obtained separately by the kerogen preparation technique, and the preparation process refers to GB/T19144-2010. Firstly, the shale samples were finely crushed to coarse grain size (18–35 mesh). Then, the samples were subjected to acid treatment using hydrochloric acid and hydrofluoric acid on a case in auto processor, followed by alkaline treatment using sodium hydroxide solution. For the Longmaxi shale, pyrite treatment with hydrochloric acid and arsenic-free zinc grains is also added. Finally, heavy liquid flotation is accomplished in a centrifuge. It should be worth noting that soluble organic matter will also occupy part of the pore space. Thus, in order to ensure the true pore structure of the organic matter, the operation of chloroform extraction of organic matter is omitted in this paper.

3.4. CO_2 and N_2 gas adsorption

The pore volumes of micropores (<2 nm), mesopores (2–50 nm), and some macropores (>50 nm) of shale can be quantitatively characterized by CO_2 and N_2 gas adsorption experiments. The samples were crushed into grains of about 60 mesh size before conducting experimental testing. Based on the range of different pore spaces that carbon dioxide and nitrogen gas molecules can enter, combined carbon dioxide and nitrogen gas adsorption experiments can effectively characterize the pore structure characteristics of micropores, mesopores, and some macropores.

3.5. Technology workflow

In this paper, a new method for calculating the critical water saturation of shale is proposed. For water-bearing shale, it is first necessary to establish a geologic model of water-bearing shale, which contains the organic-inorganic pore system of shale and takes full account of the distribution characteristics of water, and then the geologic model will be established. On the basis of the geological model, the critical water saturation of pores and shale samples can be quantitatively calculated (Fig. 3). Firstly, the critical water saturation in the pores with different pore sizes can be calculated according to the DLVO theory, and then the pore size distribution characteristics of the shale and its corresponding pore size distribution characteristics of the organic matters can be obtained by the kerogen preparation technique and the gas adsorption experiments of CO_2 and N_2. After the gas adsorption curves of the kerogen samples were standardized, the pore size distribution characteristics of the inorganic pores in the shale and the percentage of the inorganic pore volume could be obtained based on the gas adsorption curves of the shale samples and the gas adsorption curves of the standardized kerogen samples. Then, the critical water saturation of the inorganic pores of the shale samples can be obtained by combining the pore size distribution characteristics of the inorganic pores and the calculation results of the critical water saturation of every single pore. Finally, according to the percentage of inorganic pore volume, the critical water saturation of shale samples can be obtained.

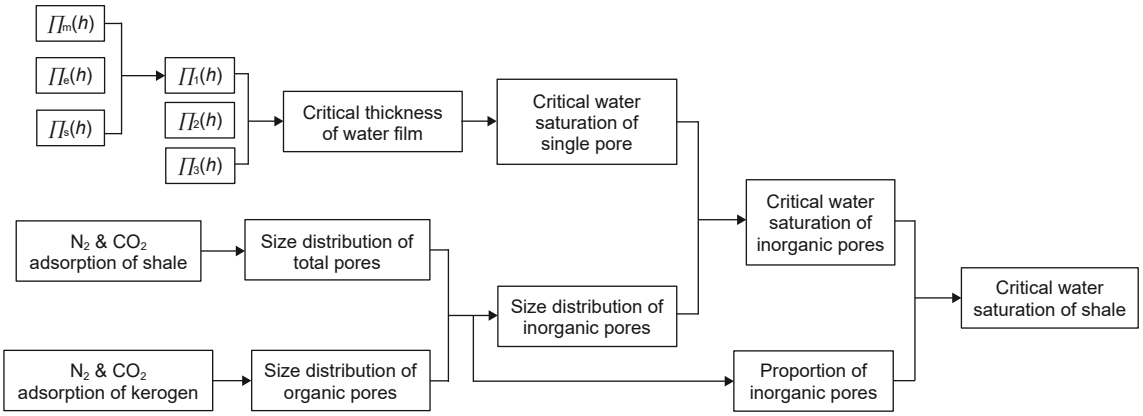

Fig. 3. The workflow for calculating the critical water saturation of shale.

4. Results and discussion

4.1. Morphological characteristics of pores and geological modeling

4.1.1. Morphological characteristics of pores

The organic and inorganic components of shale can be distinguished by binarization processing in the pictures (Fig. 4(a), (b), (e), (f)). There is a clear difference between the percentage of organic and inorganic fractions in the two groups of shale simples under the large field of view. The organic matter content of N2 sample is significantly higher than that of N1 sample. After the scanning electron microscope images were binarized, it was found that the proportion of organic matter of N1 was 0.50% and that of N2 was 5.04% (Fig. 4(b)–(f)). The proportion of organic matter of N2 was about 10 times of N1, and this great difference may lead to a very different distribution of water in the two shale samples.

In addition, a large number of organic and inorganic pores can be observed in a small field of view. Organic pores are intragranular pores developed inside the organic matter of shale which are usually easy to recognized. A large number of honeycomb-like bubble pores, mainly circular and elliptical, with pore diameters ranging from a few nanometers to hundreds of nanometers, can be observed in N2 samples (Fig. 4(g)), presenting the phenomenon of large pores over small pores, which is a type of pore with the best connectivity. Organic pores can also be observed in the N1 sample, and the pore morphology is also dominated by round and oval shapes, but there are not many organic pores (Fig. 4(c)), which may be due to the fact that the TOC of the N1 is very low, and thus the hydrocarbon generation ability is weak, resulting in the development of organic pores in the N1 sample is not as good as that of the N2. The inorganic pores mainly include intergranular pores, intragranular pores and microcracks. The inorganic pores that can be observed under the microscope are mainly developed in clay minerals, and due to the laminated structure of clay minerals, a large number of slit-like pores are developed between the clay minerals as well as within the layers of clay minerals (Fig. 4(d)–(h)). Some irregular intra-granular dissolution pores (Fig. 4(h)) were also observed in other detrital particles (possibly carbonate minerals such as feldspar or calcite), as well as the development of microcracks that can be observed between some brittle mineral particles (Fig. 4(d)–(h)).

4.1.2. Geological models of water-bearing shale

In order to calculate the critical water saturation of shale, we need to establish a simplified geologic model of water-bearing shale. First, through scanning electron microscopy observation, it can be found that the organic matter pores of shale are mainly round and elliptical in shape. The inorganic pores include slit pores, dissolution pores, and microcracks, which are dominated by slit pores in clay minerals. Therefore, the morphological characteristics of organic and inorganic pores in shale can be simplified to capillary pores and slit pores (Fig. 5), which can be well applied to the

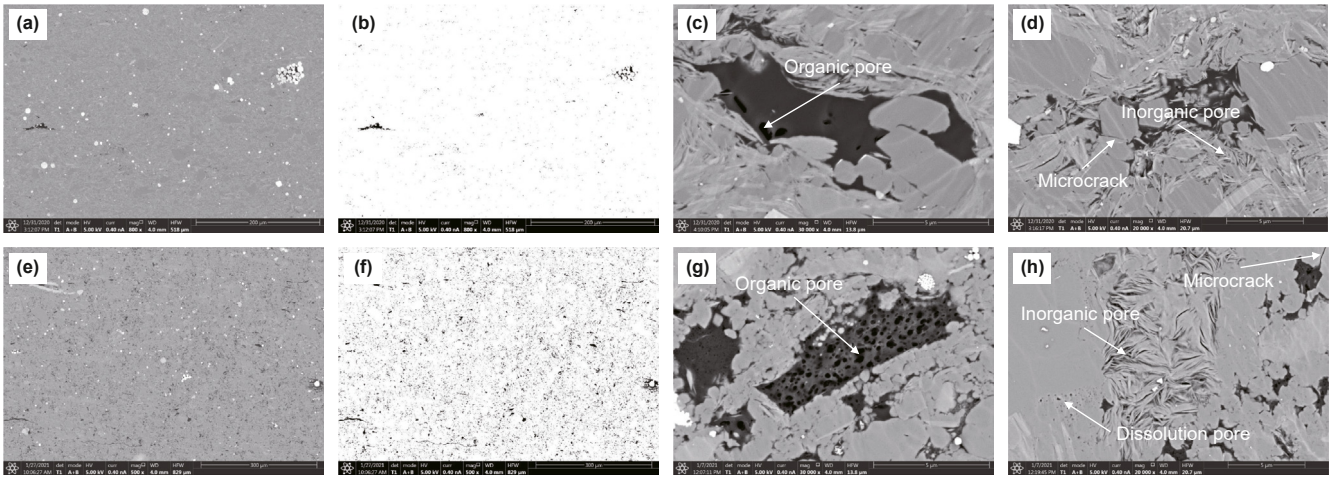

Fig. 4. FE-SEM photos of shale samples. **(a)** and **(b)** are original and corresponding binarized photos of N1 simple. **(e)** and **(f)** are original and corresponding binarized photos of N2 simple. **(c)** and **(g)** are organic pore photos of N1 and N2 simples. **(d)** and **(h)** are inorganic pore and microcrack photos of N1 and N2 simples.

theoretical model of water film thickness.

Second, the distribution pattern of water also needs to be considered. Kelvin's thermodynamic equation shows that water usually condenses preferentially in small pores and then aggregates in large pores, meanwhile, water is mainly distributed in the pores of hydrophilic clay minerals; and lastly, due to the fact that organic matter requires water consumption for hydrocarbon generation, and at the same time, the oil and gas generated during the hydrocarbon generation process will carry water outward (Xue et al., 2015), the percentage of water in the organic matter will be ignored in our study. Molecular simulation studies have shown that only a small amount of water in shale aggregates on the surface of kerogen in Longmaxi shale to form unstable clusters, and when methane flows, it will move to the surface or port of clay minerals and fuse with water in inorganic pores (Huang et al., 2024). Meanwhile, previous studies have analyzed through experiments that only 30% of the organic micropores in the Longmaxi shale may contain water (Cheng et al., 2018, 2019, 2022). According to the pore structure data of the samples in our study, it is calculated that the average water saturation of organic pores in shale is only 4.58%. Therefore, the water in the organic pores of shale can be ignored. With the above principles, a simplified geologic model of water-bearing shale was developed. As shown in Fig. 6, there are organic and inorganic pores of different pore sizes in the shale geologic model. It is assumed that there is no water in organic pores. And, in the case of inorganic pores, the presence of water in micropores is in the form of capillary water due to capillary condensation, while the presence in macropores is in the form of water film. The inorganic pore porous model consists of multiple inorganic pore single pore models. Since the critical water saturation varies in pores with different sizes, the critical water saturation of the porous model and the shale model can be obtained by weighted summation.

4.2. Pore structure characteristics

4.2.1. Pore size distribution

The pore size distribution curves of total pores, organic pores and inorganic pores of the two groups of samples were obtained by CO_2 and N_2 gas adsorption experiments and kerogen preparation technique (Fig. 7). It is worth noting that the gas adsorption experiment results of kerogen need to be corrected with TOC in order to be compared with the gas adsorption experiment results of shale samples. The pore size distribution characteristics of the two groups of shale samples are obviously different. The pore size distribution curve of the total pore space of the N1 shale sample has a primary peak and a secondary peak, the range of the primary peak is around 40 nm, and the range of the secondary peak is about 10–20 nm (Fig. 7(a)). The N1 sample is dominated by pores around 40 nm. The pore size distribution curve of the total pores of the N2 shale sample is a bimodal characteristic, and the distribution range of the two peaks is the same as that of the N1 shale sample. But the pores of 10–20 nm as well as the pores around 40 nm are both the dominant pores of the N2 shale sample (Fig. 7(d)). The pore distribution characteristics of organic matter in N1 shale sample exhibit obvious unimodal characteristics. From the distribution curve of the organic matter pores, there is only one obvious peak at around 40 nm in the N1 sample (Fig. 7(b)), while the pore size distribution of organic pores in N2 shale samples exhibits the same bimodal characteristics as the total pores of shale. But the height of the peak is significantly higher than that of the N1 sample (Fig. 7(e)). On the one hand, shale with higher TOC develops more organic pore volume. On the other hand, more micropores and smaller mesopores developed in the shale with higher TOC. This indicates that the value of TOC of shale not only affects the size of the organic pore volume, but also affects the developmental characteristics of the organic pores. The difference between the total pores of shale and organic pores size distribution curves is the pore size distribution curve of inorganic pores (Fig. 7(c)–(f)). The inorganic pore size distribution curves of both samples show bimodal characteristics with inorganic pores of sample N1 being more developed relative to N2. But in the same way, inorganic micropores and smaller inorganic mesopores seem to be more predominant in sample N2, suggesting the synergistic evolution of the inorganic pores with the organic pores. It is worth noting that the

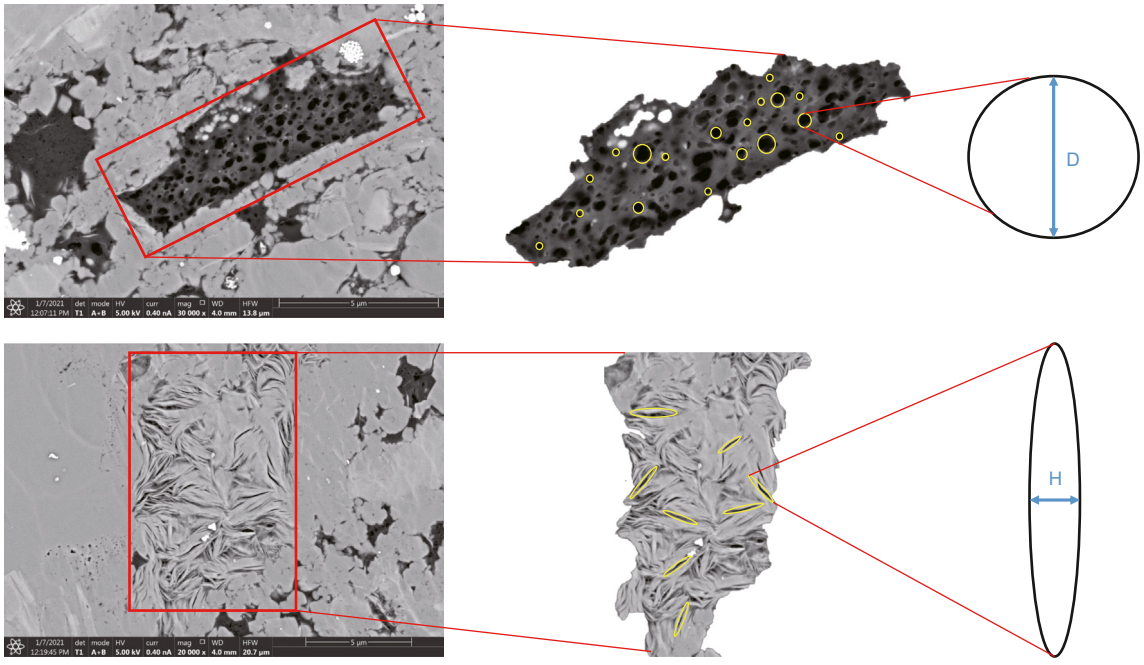

Fig. 5. Simplified schematic diagram of pore morphology for organic and inorganic pores.

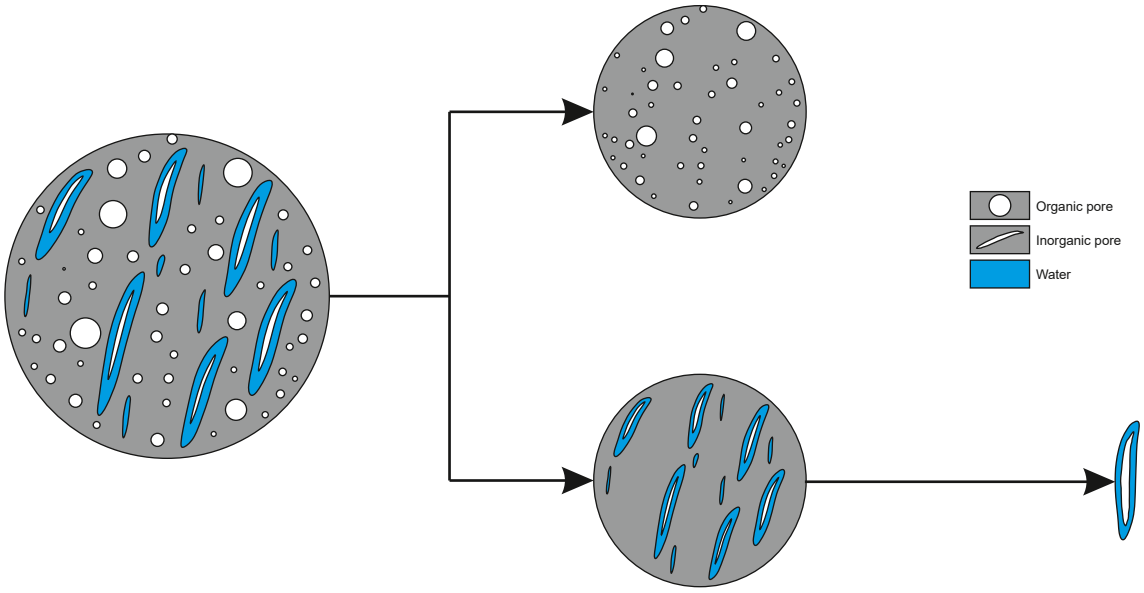

Fig. 6. Geological models of organic and inorganic pores of water-bearing shale.

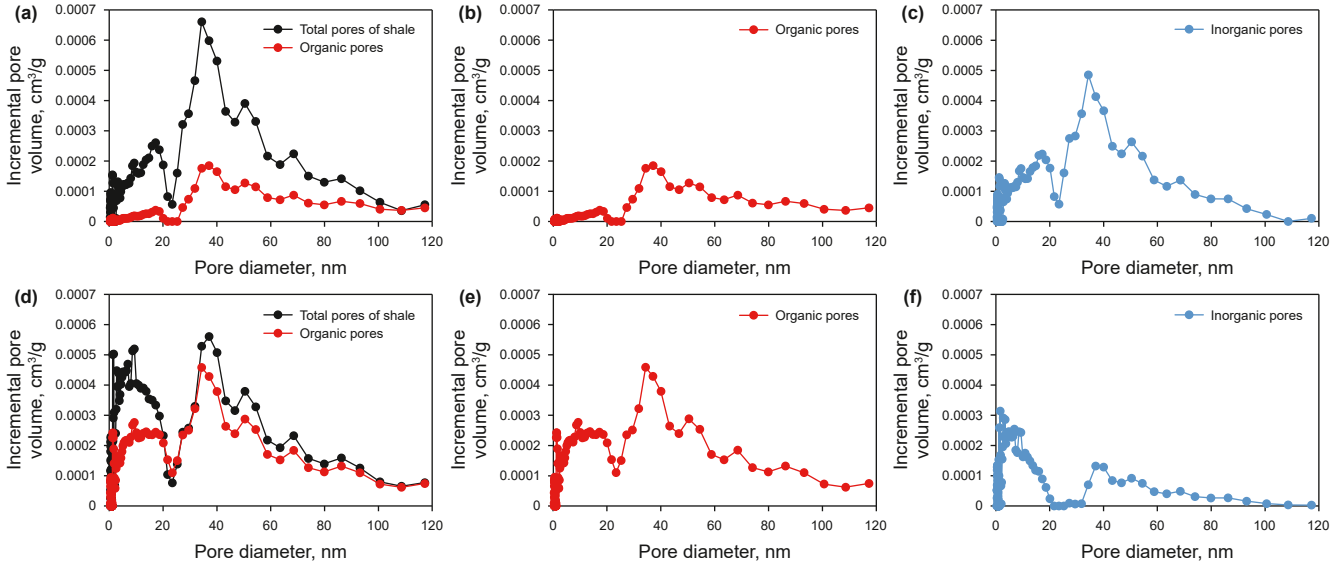

Fig. 7. Pore size distribution map. **(a)**, **(b)** and **(c)** are pore size distribution curves of total pores, organic pores and inorganic pores of N1 samples. **(d)**, **(e)** and **(f)** are pore size distribution curves of total pores, organic pores and inorganic pores of N2 samples.

values of several data points in the organic pore size distribution curve are slightly smaller than the values of the corresponding data points of total pores, which might be an error caused by the process of processing the sample and adsorption data. In this case, we have taken the default value of 0. Based on the inorganic pore size distribution curves, we can calculate and weight the critical water saturation of each inorganic pore.

4.2.2. Percentage of organic and inorganic pores

The critical water saturation of shale can be obtained by combining the critical water saturation of inorganic pores and the pore volume percentage of inorganic pores. The pore volume percentage of inorganic pores was obtained from the cumulative pore volume curves of the shale samples and their OM samples. Inorganic pores dominate the N1 sample with lower TOC, in which the organic pores accounted for 19.0% and the inorganic pores accounted for 81.0% (Fig. 8(a)). Compared with the N1 sample, the organic pores in the N2 sample accounted for a higher percentage of pore volume. The organic pores and inorganic pores accounted for 51.3% and 48.7% (Fig. 8(b)). In addition, the TOC of the shale directly affected the development of the total pores and organic pores volume of the shale while it did not have a significant effect on the development of inorganic pores. The total pores volume of the N1 sample was 0.0125 cm^3/g, with an organic pores volume of 0.0024 cm^3/g and an inorganic pores volume of 0.0101 cm^3/g, while the total pores volume of N2 sample is 0.0275 cm^3/g, with an organic pores volume of 0.0141 cm^3/g, and the inorganic pores volume is 0.0134 cm^3/g. The difference in total pores volume between N1 and N2 samples is mainly caused by organic pores, which contribute 78%, and the variation of inorganic pores is small. The

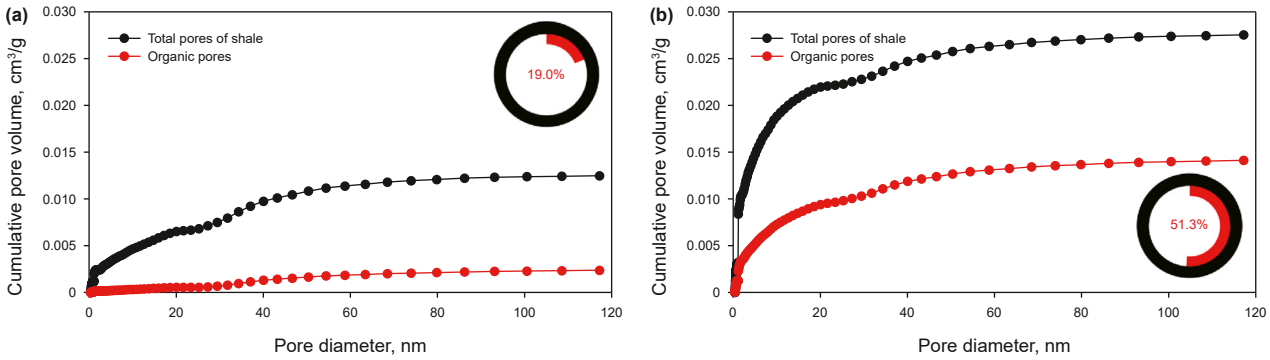

Fig. 8. Cumulative pore volume curves of total pores and organic pores of shale samples. **(a)** N1 sample, **(b)** N2 sample.

differences in pore structure are likely to lead to differences in the occurrence of water in the pores, so the critical water saturation of shale samples with different TOC should not be the same.

4.3. The critical water saturation of single pores

Combining the wettability differences between organic and inorganic pores of shale, water distribution characteristics, and the process of hydrocarbon generation and drainage, the slit pore model is chosen to calculate the critical water saturation for each inorganic pore. And the water saturation of organic pores is defaulted to zero. First, the thicknesses and disjoining pressures of water film in the slit pores with different sizes can be calculated by associating Eqs. (1)–(7) and Eqs. (9)–(12). Then, the critical water film thickness when capillary condensation occurs in the inorganic slit pores of different apertures can be derived from Eq. (13), and further, the critical water saturation of the slit pores of different apertures can be obtained by the volume proportion critical water film thickness. As shown in Fig. 9(a), although the water film disjoining pressure in the plane always decreases with the increase of the water film thickness, there is an inflection point of the water film disjoining pressure in the slit pore model. This is because as the water film gradually thickens, the interaction force between the water film and pore wall in the same side gradually weakens, and the interaction force with the wall and water film in the opposite side gradually increases, ultimately leading to the loss of water film stability. The water film in the slit pores of different pore sizes will lose its stability when it reaches a certain thickness, and then immediately form the capillary condensation phenomenon. The slit pores of different pore sizes have their own critical water film thickness and critical water saturation. For example, the critical water film thickness is 0.65 nm and critical water saturation is 65% in 2 nm pore (Fig. 9(b)); the critical water film thickness is 1.8 nm and critical water saturation of 72% in 5 nm pore (Fig. 9(c)); the critical water film thickness is 3.8 nm and critical water saturation of 76% in 10 nm pore (Fig. 9(d)); the critical water film thickness is 7.3 nm and critical water saturation of 73% in 20 nm pore (Fig. 9(e)) and the critical water film thickness is 16 nm and critical water saturation of 64% in 50 nm pore (Fig. 9(f)).

In general, as the pore size of the inorganic pores increases, the corresponding critical water film thickness also increases. However, an interesting phenomenon is that the critical water saturation does not increase with the increase of pore size (Fig. 10(a)), but it exhibits normal distribution characteristics within the aperture range centered around about 10 nm. The distribution of the critical water saturation when capillary condensation occurs in inorganic pores of different pore sizes ranges from 63% to 76% (Fig. 10(b)). In a complex separation pressure field, the critical water saturation of

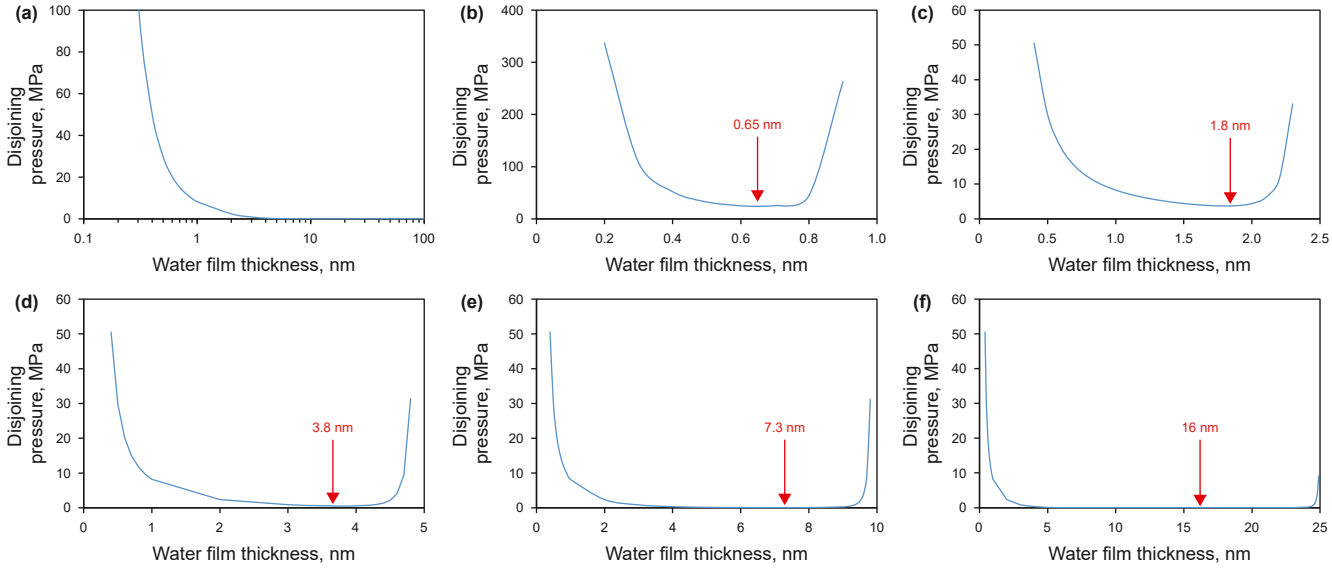

Fig. 9. Critical water film thickness of slit pores with different widths. **(a)** Flat surface, **(b)** 2 nm slit pore, **(c)** 5 nm slit pore, **(d)** 10 nm slit pore, **(e)** 20 nm slit pore and **(f)** 50 nm slit pore.

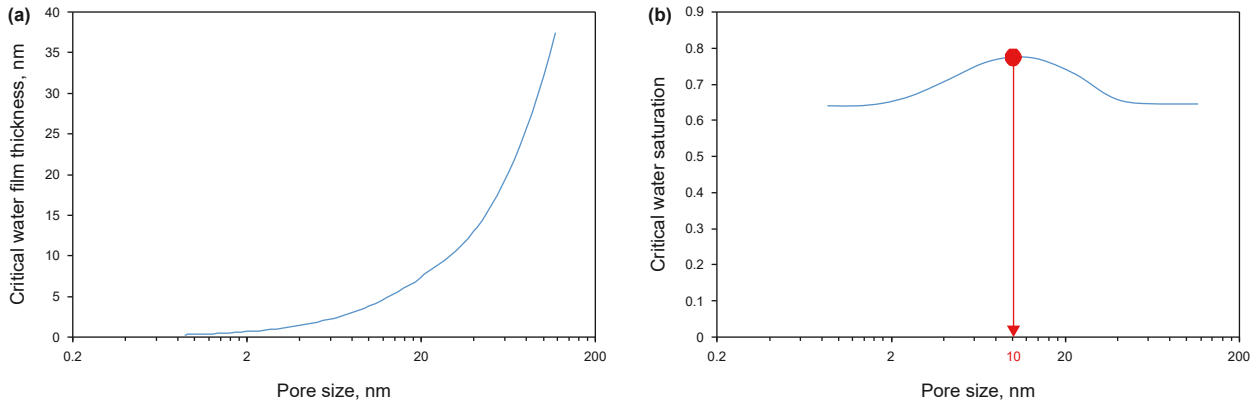

Fig. 10. Critical water film thickness **(a)** and critical water saturation **(b)** of slit pore with different widths.

different pore sizes varies by about 13%. So, the critical water saturation differed by at most 13% if only the effect of pore size distribution characteristics was considered. The percentage of inorganic pores in the two sets of shale samples in this paper differed by 32.3%. This value is even larger when the TOC difference is greater (Zhang et al., 2017a; Zhang et al., 2020). This suggests that the effect of pore size distribution characteristics on the critical water saturation of shale may be smaller than the effect of the difference in the percentage of inorganic pores on the critical water saturation of shale.

4.4. Critical water saturation of shale samples

4.4.1. Boundary conditions of the geological model

Based on the pore size distribution characteristics of the inorganic pores, the percentage of inorganic pores, and the results of the critical water saturation calculations for single pores, the total critical water saturation of the shale samples can be calculated. In addition, there are several boundary conditions that need to be set before the final calculation. ①The DLVO theory will be used to calculate the critical water saturation of pores with pore size less than or equal to 30 nm. The pore size distribution range of the connecting pore throats within the Longmaxi shale was characterized by previous researchers based on FIB-SEM and FIB-HIM experiments, and it was clarified that the diameter of the connecting pore throats in the Longmaxi Formation is mainly distributed between 10 and 30 nm (Wu et al., 2020). Therefore, 30 nm is defined as the maximum connecting pore diameter in this study, i.e., when pore water gradually fills up to 30 nm, the shale can form an effective closure capacity; ②Water saturation in the pores with pore diameters larger than 30 nm is calculated based on a single-layer water film; ③The water saturation in pores with pore diameters less than 7.5 nm is defaulted to 100%. Previous N_2 adsorption experiments carried out on clay mineral particle samples at different humidity levels found that the pores below 7.5 nm in clay minerals have been completely filled with water at low humidity levels (corresponding to lower water saturation). This means that this portion of the pore space is already completely filled with water by the time the shale forms its sealing capacity (Li et al., 2016; Feng et al., 2018; Zhu et al., 2021); ④The water saturation of micropores with the pore diameter of 1.2 nm or less is calculated as on the basis of individual water molecule layers. The water in inorganic micropores with the pore size less than 1.2 nm is usually the water contained in clay mineral interlayers. The number of water molecule layers contained in the clay mineral interlayer can be judged by the valence of the interlayer cation. If the interlayer cation is Ca^{2+}, there exist two water molecule layers in the interlayer, and if it is Na^{+}, then there is generally only one water molecule layer in the interlayer (Li et al., 1986). As it has been pointed out previously that the formation water of Longmaxi shale is mainly of NaCl type, so the water saturation of pores below 1.2 nm are calculated as a single water molecule layer case.

4.4.2. Critical water saturation of shale samples

Finally, we calculated the critical water saturation for the two shale samples. The critical water saturation for the N1 shale sample is about 41.7% and that for the N2 sample is about 32.7%, with a difference of about 10% between the two sets of shale samples. This result is in line with our expectation. On the one hand, the critical water saturation is definitely not the same for different shales when their effective sealing capacity are formed, which is affected by the ratio of organic and inorganic components and the pore size distribution characteristics of inorganic pores. And it can be clearly observed that for shale with high TOC, the critical water saturation is relatively low. On the other hand, the method proposed in this study accurately calculates the critical water saturation of shales and effectively distinguishes the differences between shales, indicating that the present method is superior to physical simulation experiments.

4.4.3. Models for water-bearing shale

Based on the calculation results, two different models of water-bearing shale were established (Fig. 11). Shale samples represented by N1 shale exhibit characteristics of lower TOC, higher content of inorganic components (mainly clay minerals), and higher proportion of inorganic pores. The fluid in the pores is mainly water (Fig. 11(a)). And the shale represented by the N2 shale sample is characterized by higher content of organic components and more developed organic pores (Fig. 11(b)). The fluid in the pores is mainly gas. Typically, the first type of shale requires a higher water saturation to form an effective sealing capacity, while the second type of shale requires a lower water saturation to form an effective sealing capacity because the inorganic pores is not dominant.

4.5. Validation of calculation results

Previous studies have been carried out on the critical water saturation of the water film when capillary condensation occurs in the single pore model in terms of both water film theory and molecular dynamics simulations. Tuller et al. (1999) suggested that intermolecular forces dominate the behavior of the water film in single pores. The disjoining pressure in the slit pore model is further simplified only when considering intermolecular interactions. The critical water film thickness for capillary

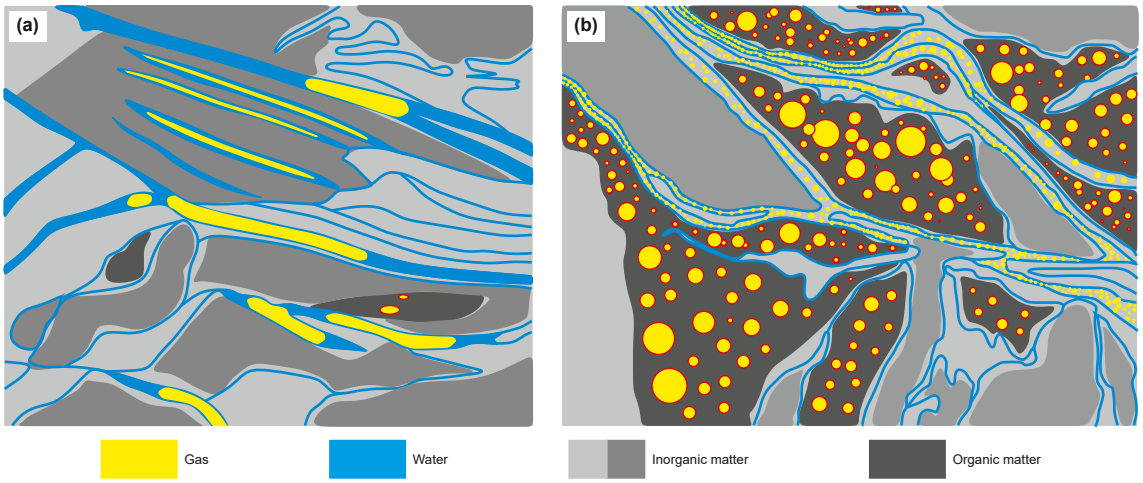

Fig. 11. Models of water-bearing shale with low TOC **(a)** and high TOC **(b)**.

condensation of water film in slit pores can be obtained by taking derivatives, which is approximately H/3, corresponding to a critical water saturation of approximately 66.7%. In addition, molecular dynamics simulation is an effective method to study the behavior of water film at the nanoscale. The occurrence state of water in the nanopore under different water saturation conditions can be analyzed by establishing a nanopore model and inserting different numbers of water molecules and methane molecules into the pores, selecting a suitable force field, and observing the distributions of water molecules and methane molecules after the system reaches equilibrium under the equilibrium molecular dynamics simulation. The results of simulation calculation show that the critical water saturation corresponding to capillary condensation of water film in a 6 nm hydrophilic slit pore is 59.4% (Xu et al., 2020; Yu et al., 2021). Calculation results in our study show that the critical water content saturation corresponding to capillary condensation of water film occurring in hydrophilic slit pore model is 63%–76%, which are consistent with the result of simplified model of water film theory. However, the critical water saturation of the 6 nm slit pore in our study is 73.0%, which is very different from the results of molecular dynamics simulation. This may be related to the model established in molecular dynamics simulation software. As well as there is a difference in the nature of the water, the water in the molecular dynamic simulation is pure water, while the water in our study is formation water. Of course, molecular dynamics simulation is still one of the most effective tools. And we need to perform more targeted validation at a later stage.

Although physical simulation methods have significant uncertainties in measuring the critical water saturation of dense rocks, general trends can be obtained. In order to validate the critical water saturation calculations for shale, breakthrough pressures at different water saturations for multiple sets of N1 and N2 shale column samples were tested by step-by-step method (Wu et al., 2020). The test results are shown in Fig. 12. The breakthrough pressures of the N1 shale samples increase rapidly in the interval of water saturation about 40%–60%, and the breakthrough pressures of the N2 shale samples increase rapidly in the interval of water saturation about 30%–50%. Our theoretical calculations are relatively small, but they are all within the range of the measured critical water saturation. In addition, the critical water saturation interval of the N1 shale samples is about 10% higher than that of the N2 shale samples, which is also close to the difference of the two samples from our theoretical calculation results. This fully verifies the reasonableness of our theoretical calculation results.

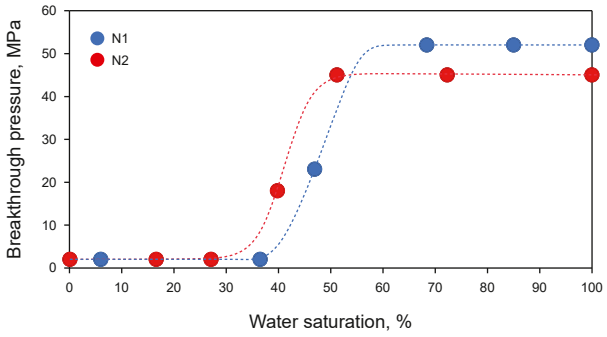

Fig. 12. Breakthrough pressure for two shale samples.

However.it is worth noting that the test results of the physical simulation experiment are obtained after a large amount of testing, which requires a large amount of shale samples, testing time, and experimental funds, so the method proposed in this paper is simpler and more efficient compared to physical simulation experiments.

4.6. Significance of critical water saturation

Critical water saturation is defined as the water saturation of shale when it forms an effective sealing capacity for gas in this paper. In actual geologic situations, shale formations contain some amount of primary water. The primary water saturation of shale may be higher or lower than the critical water saturation. When the primary water saturation of the shale is higher than the critical water saturation, the shale formation forms an effective sealing to the gas, which prevents the gas inside the shale from dissipating to the outside as well as preventing the gas from passing through the shale formation. In this case, shale can serve as an effective cap rock in the gas reservoir and form an overpressure fluid storage box. And when the primary water saturation of shale is lower than the critical water saturation, water occupies less space in the shale pores, and the shale can serve as a reservoir for gas. Therefore, by calculating the critical water saturation of different shales and comparing it with the primary water saturation of shales can identify the cap and reservoir layers in the shale gas play, so as to accurately locating the target and further guide the exploration and development of shale gas. This places higher demands on the

calculation of primary water saturation and critical water saturation. Therefore, in this article, we propose a new method for more convenient and accurate calculation of critical water saturation. Meanwhile, the method can also be applied to the field of CCUS, such as calculating the adsorbed water film thickness in CO_2 gas reservoirs based on the DLVO theory and evaluating the capping capacity of the cap layer in CO_2 gas reservoirs (Tokunaga, 2012). In conclusion, the calculation method of critical water saturation has obvious advantages and has a wide range of applications. The prediction of critical water saturation for different shales and the fine analysis of shale gas reservoirs by comparing the critical water saturation with the original water saturation will be the next step of our research.

5. Conclusions

(1) An effective method is proposed to quantitatively calculate the critical water saturation when shale forms effective sealing capacity based on the DLVO theory and the characterization method of rock pore structure characteristics.
(2) Shale with a TOC of 0.89% has 81.0% of inorganic pores, and the dominant pore sizes are dominated by mesopores around 40 nm, while shale with a TOC of 4.27% has 48.7% of inorganic pores, and the dominant pore sizes are dominated by micropore and mesopore sizes of 0–20 nm and 40 nm.
(3) As the pore size increases, the corresponding critical water film thickness also increases. The critical water saturation is normally distributed in the pore size range centered at about 10 nm. And the critical water saturation of inorganic pores ranges from 63% to 76%. The critical water saturation of shale with a TOC of 0.89% and shale with a TOC of 4.27% were calculated to be 41.7% and 32.7%, respectively.
(4) By comparing the critical water saturation of shale with the original water saturation, it is possible to provide a fine description of shale gas reservoirs and guide the exploration and development of shale gas. And it can also be applied to the field of CCUS for CO_2 geological storage evaluation.

CRediT authorship contribution statement

Cheng-Xiang Wan: Writing – original draft, Methodology, Investigation, Formal analysis, Conceptualization. **Xu-Sheng Guo:** Validation, Supervision, Conceptualization. **Bao-Jian Shen:** Project administration, Methodology. **Yan Song:** Supervision, Resources. **Peng-Wei Wang:** Data curation. **Ru-Yue Wang:** Writing – review & editing, Visualization.

Declaration of competing interest

The authors declare that they have no known competing financial interests or personal relationships that could have appeared to influence the work reported in this paper.

Acknowledgments

Sincerely thanks to the support provided by the Sinopec Ministry of Science and Technology Research Project of Experimental study and application of key parameters for self-sealing evaluation of deep shale (KLP25015), Research on stress in complex tectonic zones and its impact on shale gas enrichment and high yield (P24181), Quantitative characterization technology and application of fluid properties in veins of shale of eastern fault basins (KLP24017) and Evolution and differential enrichment mechanism of deep–ultra deep shale gas in southeastern Sichuan (P23132).

References

Bucior, K., 2004. Capillary condensation of a model binary mixture in slit-like pores with differently adsorbing walls. Colloids Surf. A Physicochem. Eng. Asp. 243 (1), 105–115. https://doi.org/10.1016/j.colsurfa.2004.05.008.
Cai, X., Zhou, D., Zhao, P., et al., 2023. Development progress and outlook of deep and normal pressure shale gas of SINOPEC. Petroleum Geology & Experiment. 45 (6), 1039–1049. https://doi.org/10.11781/sysydz2023061039.
Charrière, D., Behra, P., 2010. Water sorption on coals. J. Colloid Interface Sci. 344 (2), 460–467. https://doi.org/10.1016/j.jcis.2009.11.064.
Cheng, P., Xiao, X., Tian, H., et al., 2018. Water content and equilibrium saturation and their influencing factors of the Lower Paleozoic overmature organic-rich shales in the Upper Yangtze Region of Southern China. Energy Fuels 32, 11452–11466. https://doi.org/10.1021/acs.energyfuels.8b03011.
Cheng, P., Xiao, X., Wang, X., et al., 2019. Evolution of water content in organic-rich shales with increasing maturity and its controlling factors: implications from a pyrolysis experiment on a water-saturated shale core sample. Mar. Petrol. Geol. 109, 291–303. https://doi.org/10.1016/j.marpetgeo.2019.06.023.
Cheng, P., Wu, W., Gao, H., 2022. Distribution and phases of pore water in overmature marine shale nanopores: a theoretical calculation model based on the pore water content of as-received shale samples. Geochimica 51 (5), 503–515. https://doi.org/10.19700/j.0379-1726.2022.05.002.
Churaev, N.V., 1995. Contact angles and surface forces - ScienceDirect. Adv. Colloid Interface Sci. 58 (2–3), 87–118. https://doi.org/10.1016/0001-8686(95)00245-L.
Churaev, N.V., Starke, G., Adolphs, J., 2000. Isotherms of capillary condensation influenced by formation of adsorption films: 1. Calculation for model cylindrical and slit pores. J. Colloid Interface Sci. 221 (2), 246–253. https://doi.org/10.1006/jcis.1999.6592.
Clarkson, C.R., Bustin, R.M., 2000. Binary gas adsorption/desorption isotherms: effect of moisture and coal composition upon carbon dioxide selectivity over methane. Int. J. Coal Geol. 42 (4), 241–271. https://doi.org/10.1016/S0166-5162(99)00032-4.
Curtis, M.E., Ambrose, R.J., Sondergeld, C.H., Rai, C.S., 2011. Transmission and scanning electron microscopy investigation of pore connectivity of gas shales on the nanoscale. North American Unconventional Gas Conference and Exhibition. 14–16 June. https://doi.org/10.2118/144391-MS the Woodlands, Texas, USA.
Davide, M., Victor, S., 2012. Sergey Semenov. Thickness, stability and contact angle of liquid films on and inside nanofibres, nanotubes and nanochannels. J. Colloid Interface Sci. 384 (1), 149–156. https://doi.org/10.1016/j.jcis.2012.06.051.
Derjaguin, B.V., Landau, L., 1941. Theory of the stability of strongly charged lyophobic sols and of the adhesion of strongly charged particles in solutions of electrolytes. Acta Phys. Chim. URSS 14, 633. https://doi.org/10.1016/0079-6816(93)90013-L.
Derjaguin, B.V., Churaev, N.V., Muller, V.M., et al., 1987. Surface Forces. Springer.
Derjaguin, B.V., Churaev, N.V., 1992. Polymolecular adsorption and capillary condensation in narrow slit pores. Prog. Surf. Sci. 40 (1), 173–191. https://doi.org/10.1016/0079-6816(92)90045-J.
Feng, D., Li, X., Li, J., et al., 2018. Water adsorption isotherm and its effect on pore size distribution of clay minerals. J. China Univ. Petroleum (Edition of Nat. Sci.) 42 (2), 110–118. https://doi.org/10.3969/j.issn.1673-5005.2018.02.013 (in Chinese).
Gasparik, M., Bertier, P., Gensterblum, Y., et al., 2014. Geological controls on the methane storage capacity in organic-rich shales. Int. J. Coal Geol. 123 (2), 34–51. https://doi.org/10.1016/j.coal.2013.06.010.
Gao, P., Xiao, X., Hu, D., et al., 2022. Water distribution in the ultra-deep shale of the wufeng–longmaxi formations from the Sichuan Basin. Energies 15 (6), 2215. https://doi.org/10.3390/en15062215.
Gregory, J., 1975. Interaction of unequal double layers at constant charge. J. Colloid Interface Sci. 51 (1), 44–51. https://doi.org/10.1016/0021-9797(75)90081-8.
Gu, X., Mildner, D.F.R., Cole, D.R., 2016. Quantification of organic porosity and water accessibility in Marcellus shale using neutron scattering. Energy Fuels 30 (6), 4438–4449. https://doi.org/10.1021/acs.energyfuels.5b02878.
Guo, X., Hu, D., Yu, L., et al., 2023. Study on the micro mechanism of shale self-sealing and shale gas preservation. Petroleum Geology & Experiment 45 (5), 821–831. https://doi.org/10.11781/sysydz202305821.
Guo, X., Shen, B., Li, Z., et al., 2024. Discussion on the uniformity of shale oil and gas in China. Petroleum Geology & Experiment 46 (5), 889–905. https://doi.org/10.11781/sysydz202405889.
Hough, D.B., White, L.R., 1980. The calculation of hamaker constants from liftshitz theory with applications to wetting phenomena. Adv. Colloid Interface Sci. 14 (1), 3–41. https://doi.org/10.1016/0001-8686(80)80006-6.
Hu, Y., Devegowda, D., Striolo, A., 2014. Microscopic dynamics of water and hydrocarbon in shale–kerogen pores of potentially mixed wettability. SPE J. 20 (1), 112–124. https://doi.org/10.2118/167234-PA.
Hu, Y., Devegowda, D., Striolo, A., 2015. The dynamics of hydraulic fracture water confined in nano–pores in shale reservoirs. Unconv. Oil Gas Resour. 9, 31–39. https://doi.org/10.1016/j.juogr.2014.11.004.
Hu, Z., Liu, Z., Du, W., et al., 2024. Key geological factors governing sweet spots in the Wufeng-Longmaxi shales of the Sichuan Basin, China. Energy Geoscience 5 (3), 100268. https://doi.org/10.1016/j.engeos.2023.100268.
Hua, Z., Li, M., Lin, M., et al., 2015. Characterization of sandstone surface wettability by surface potential. Journal of China University of Petroleum (Editon of Natural Science) 39 (2), 142–150. https://doi.org/10.3969/j.issn.1673-5005.2015.02.023

(in Chinese).
Huang, L., Yang, Q., Wu, J., et al., 2024. Microscopic mobilization mechanism of gas and water in deep shale nanopores. Nat. Gas. Ind. 44 (1), 139–148. https://doi.org/10.3787/j.issn.1000-0976.2024.01.013.
Hunter, R.J., Wright, H., 1971. The dependence of electrokinetic potential on concentration of electrolyte. J. Colloid Interface Sci. 37 (3), 564–580. https://doi.org/10.1016/0021-9797(71)90334-1.
Hunter, R.J., 1981. Zeta Potential in Colloid Science: Principles and Applications. Academic Press. https://doi.org/10.1016/0021-9797(82)90296-X.
Iwamatsu, M., Horii, K., 1996. Capillary condensation and adhesion of two wetter surfaces. J. Colloid Interface Sci. 182 (2), 400–406. https://doi.org/10.1006/jcis.1996.0480.
Israelachvili, J.N., 2011. Intermolecular and surface forces. Intermolecular and Surface Forces, third ed. Third Edition, pp. 381–413. https://doi.org/10.1016/b978-0-12-375182-9.10016-8.
Jiao, X., He, W., Tian, Z., et al., 2025. Characterization of water micro-distribution behavior in shale nanopores: a comparison between experiment and theoretical model. Advances in Geo-Energy Research 15 (1), 79–86. https://doi.org/10.46690/ager.2025.01.08.
Li, C., Somasundaran, P., 1991. Reversal of bubble charge in multivalent inorganic salt solutions—effect of magnesium. J. Colloid Interface Sci. 146 (1), 215–218. https://doi.org/10.1016/0021-9797(91)90018-4.
Li, J., Li, X., Li, Y., et al., 2015. Model for gas transport in nanopores of shale and tight formation under reservoir condition. Chin. Theor. Appl. Mech. 47 (6), 932–944. https://doi.org/10.6052/0459-1879-15-185.
Li, J., Li, X., Wang, X., et al., 2016a. Water distribution characteristic and effect on methane adsorption capacity in shale clay. Int. J. Coal Geol. 159, 135–154. https://doi.org/10.1016/j.coal.2016.03.012.
Li, J., Li, X., Wang, X., et al., 2016b. A quantitative model to determine water saturation distribution characteristics inside shale inorganic pores. Acta Petrol. Sin. 37 (7), 903–913. https://doi.org/10.7623/syxb201607009.
Li, J., Li, X., Wu, K., et al., 2017. Thickness and stability of water film confined inside nanoslits and nanocapillaries of shale and clay. Int. J. Coal Geol. 179, 253–268. https://doi.org/10.1016/j.coal.2017.06.008.
Li, J., Wang, S., Lu, S., et al., 2019. Microdistribution and mobility of water in gas shale: a theoretical and experimental study. Mar. Petrol. Geol. 102, 496–507. https://doi.org/10.1016/j.marpetgeo.2019.01.012.
Li, P., Yuan, W., Lin, H., et al., 1986. Discussion on factors influencing interlayer spacing variation of montmorillonite. Bull. Nanjing Inst. Geol. Miner. Resour. Chin. Acad. Geol. Sci. 7 (1), 61–76.
Li, X., Chen, S., Wu, J., et al., 2023. Microscopic occurrence and movability mechanism of pore water in deep shale gas reservoirs: a typical case study of the Wufeng Longmaxi Formation, Luzhou block, Sichuan Basin. Mar. Petrol. Geol. 151, 106205. https://doi.org/10.1016/j.marpetgeo.2023.106205.
Liu, Y., Zeng, J., Qiao, J., et al., 2023. An advanced prediction model of shale oil production profile based on source-reservoir assemblages and artificial neural networks. Appl. Energy 333, 120604. https://doi.org/10.1016/j.apenergy.2022.120604.
Nikolai, V.C., Gerhard, S., Jürgen, A., 2000. Isotherms of capillary condensation influenced by formation of adsorption films: 1. Calculation for model cylindrical and slit pores. J. Colloid Interface Sci. 221 (2), 246–253. https://doi.org/10.1006/jcis.1999.6592.
Prieve, D.C., Russel, W.B., 1988. Simplified predictions of Hamaker constants from Lifshitz theory. J. Colloid Interface Sci. 125 (1), 1–13. https://doi.org/10.1016/0021-9797(88)90048-3.
Rodríguez, K., Araujo, M., 2006. Temperature and pressure effects on zeta potential values of reservoir minerals. J. Colloid Interface Sci. 300 (2), 788–794. https://doi.org/10.1016/j.jcis.2006.04.030.
Ross, D.J.K., Bustin, R.M., 2009. The importance of shale composition and pore structure upon gas storage potential of shale gas reservoirs. Mar. Petrol. Geol. 26 (6), 916e927. https://doi.org/10.1016/j.marpetgeo.2008.06.004.
Tan, Y., Zhang, S., Tang, S., et al., 2021. Impact of water saturation on gas permeability in shale: experimental and modelling. J. Nat. Gas Sci. Eng. 95, 104062. https://doi.org/10.1016/j.jngse.2021.104062.
Tokunaga, T.K., 2012. DLVO-based estimates of adsorbed water film thicknesses in geologic CO_2 reservoirs. Langmuir 28 (21), 8001–8009. https://doi.org/10.1021/la2044587.
Tuller, M., Or, D., Dudley, L.M., 1999. Adsorption and capillary condensation in porous media: liquid retention and interfacial configurations in angular pores. Water Resour. Res. 35 (7), 1949–1964. https://doi.org/10.1029/1999WR900098.
Verwey, E.J.W., Overbeek, J., Th, G., 1948. Theory of the Stability of Lyophobic Colloids. Elsevier, Amsterdam. https://doi.org/10.1016/0095-8522(55)90030-1.
Vinogradov, J., Jackson, M.D., 2015. Zeta potential in intact natural sandstones at elevated temperatures. Geophys. Res. Lett. 42 (15), 6287–6294. https://doi.org/10.1002/2015GL064795.
Wang, R., Hu, Z., Dong, L., et al., 2021. Advancement and trends of shale gas reservoir characterization and evaluation. Oil Gas Geol. 42 (1), 54–65. https://doi.org/10.11743/ogg20210105.
Wang, R., Hu, Z., Long, S., et al., 2022. Reservoir characteristics and evolution mechanisms of the upper ordovician wufeng-lower silurian Longmaxi shale, Sichuan Basin. Oil Gas Geol. 43 (2), 353–364. https://doi.org/10.11743/ogg20220209.
Wu, J., Yuan, Y., Niu, S., et al., 2020. Multiscale characterization of pore structure and connectivity of Wufeng-Longmaxi shale in Sichuan Basin, China. Mar. Petrol. Geol. 120, 104514. https://doi.org/10.1016/j.marpetgeo.2020.104514.
Wu, J., Zhao, S., Li, B., et al., 2023. Occurrence law of pore water in shale matrix: a case study of the Silurian Longmaxi Formation in southern Sichuan Basin. Nat. Gas. Ind. 43 (7), 44–54. https://doi.org/10.3787/j.issn.1000-0976.2023.07.005.
Xing, Y.J., Xiao, X.M., Cheng, P., et al., 2024. Water adsorption performance of overmature shale and its relationship with organic and inorganic nanopores: a case study of Lower Cambrian shale from the Sichuan Basin, China. Pet. Sci. 22 (3), 977–997. https://doi.org/10.1016/j.petsci.2024.12.025.
Xu, H., Yu, H., Fan, J., et al., 2020. Two-phase transport characteristic of shale gas and water through hydrophilic and hydrophobic nanopores. Energy Fuels 34, 4407–4420. https://doi.org/10.1021/acs.energyfuels.0c00212.
Xue, B., Zhang, J., Tang, X., et al., 2015. Characteristics of microscopic pore and gas accumulation on shale in Longmaxi Formation, northwest Guizhou. Acta Pet. Sin. 36 (2), 138–149. https://doi.org/10.7623/syxb201502002, 173.
Xue, X., Li, J., Liu, H., et al., 2023. Analysis on development potential of shale gas industry in our country under the background of "dual carbon". China Energy and Environmental Protection 45 (9), 169–174. https://doi.org/10.19389/j.cnki.1003-0506.2023.09.026.
Yang, R., Jia, A., He, S., et al., 2020. Water adsorption characteristics of organic-rich wufeng and Longmaxi shales, Sichuan Basin (China). J. Petrol. Sci. Eng. 193, 107387. https://doi.org/10.1016/j.petrol.2020.107387.
Yu, H., Zhu, Y., Jin, X., et al., 2019. Multiscale simulations of shale gas transport in micro/nano-porous shale matrix considering pore structure influence. J. Nat. Gas Sci. Eng. 34 (4), 4407–4420. https://doi.org/10.1016/j.jngse.2019.01.016.
Yu, H., Xu, H., Fan, J., et al., 2021. Transport of shale gas in microporous/nanoporous media: molecular to pore-scale simulations. Energy Fuels 35 (2), 911–943. https://doi.org/10.1021/acs.energyfuels.0c03276.
Zeng, L., Lu, Y., Maskari, N., et al., 2020. Interpreting micromechanics of fluid-shale interactions with geochemical modelling and disjoining pressure: implications for calcite-rich and quartz-rich shales. J. Mol. Liq. 319 (15), 114117. https://doi.org/10.1016/j.molliq.2020.114117.
Zhao, Y., Zhang, Q., Chen, X., et al., 2021. Experimental investigation on effect of water film thickness in unsaturated sandstone cores on CO_2 transport during geologic storage. J. Hydrol. 601, 126595. https://doi.org/10.1016/j.jhydrol.2021.126595.
Zhang, C., Yu, Q., 2016. The effect of water saturation on methane breakthrough pressure: an experimental study on the Carboniferous shales from the eastern Qaidam Basin, China. J. Hydrol. 543, 832–848, 10.1016/j.jhydrol.2016.11.003.
Zhang, C., Yu, Q., 2019. Breakthrough pressure and permeability in partially water-saturated shales using methane–carbon dioxide gas mixtures: an experimental study of Carboniferous shales from the eastern Qaidam Basin, China. AAPG (Am. Assoc. Pet. Geol.) Bull. 103 (2), 273–301. https://doi.org/10.1306/07111818018.
Zhang, J., Li, X., Wei, Q., et al., 2017. Quantitative characterization of pore-fracture system of organic-rich marine-continental shale reservoirs: a case study of the Upper Permian Longtan Formation, Southern Sichuan Basin, China. Fuel 200, 272–281. https://doi.org/10.1016/j.fuel.2017.03.080.
Zhang, G., Nie, H., Tang, X., et al., 2021. Evaluation of shale gas preservation conditions based on formation water index: a case study of Wufeng-Longmaxi Formation in Southeastern Chongqing. Reservoir Evaluation and Development 11 (1), 47–55. https://doi.org/10.13809/j.cnki.cn32-1825/te.2021.01.007.
Zhang, W., Huang, Z., Li, X., et al., 2020. Estimation of organic and inorganic porosity in shale by NMR method, insights from marine shales with different maturities. J. Nat. Gas Sci. Eng. 78, 103290. https://doi.org/10.1016/j.jngse.2020.103290.
Zhu, D., Jiang, Z., Jiang, S., et al., 2021. Water-bearing characteristics and their influences on the reservoir capacity in terrestrial shale reservoirs: a case study of the lower Jurassic Ziliujing Formation in the Northeast Sichuan Basin, China. Mar. Petrol. Geol. 123, 104738. https://doi.org/10.1016/j.marpetgeo.2020.104738.
Zhu, L., Ma, Y., Cai, J., et al., 2022. Key factors of marine shale conductivity in southern China—Part II: the influence of pore system and the development direction of shale gas saturation models. J. Petrol. Sci. Eng. 209, 109516. https://doi.org/10.1016/j.petrol.2021.109516.
Zhu, L., Wu, S., Zhou, X., et al., 2023. Saturation evaluation for fine-grained sediments. Geosci. Front. 14, 101540. https://doi.org/10.1016/j.gsf.2023.101540.
Zou, J., Reza, R., Yuan, Y., et al., 2020. Distribution of adsorbed water in shale: an experimental study on isolated kerogen and bulk shale samples. J. Petrol. Sci. Eng. 187, 106858. https://doi.org/10.1016/j.petrol.2019.106858.